Analysis of the mixed secondary radiation field in proton therapy using a Timepix detector

Matamoros A[1,2†], Nabha R [1,2,3†], De Saint-Hubert M [1], Van Hoey O [1], Depuydt T [2,4], Esser J [5,6,9], Bäumer C [5,6,7,8], Verbeek N [5,6], Struelens L [1] , Vaniqui A[1], Heinzelmann F [5,6,7], Sterpin E [2,10], Brualla L[5,6], Marek L [11], Granja C [11], Oancea C [11], Timmermann B [5,6,8,9], Vanhavere F [1,2]*

[1]Radiation Protection Dosimetry and Calibration Expert Group, Belgian Nuclear Research Center (SCK CEN), Mol, Belgium
[2]KU Leuven, Department of Oncology, Laboratory of Experimental Radiotherapy, Leuven, Belgium
[3]Department of Radiotherapy, Universitair Ziekenhuis Brussel, Vrije Universiteit Brussel, Brussels, Belgium
[4]UZ Leuven, Department of Radiation Oncology, Belgium
[5]West German Proton Therapy Centre Essen, Essen, Germany
[6]West German Cancer Center (WTZ), University Hospital Essen, Essen, Germany
[7]TU Dortmund University, Department of Physics, Dortmund, Germany
[8]German Cancer Consortium (DKTK), Essen, Germany
[9]Department of Particle Therapy, University Hospital Essen, Essen, Germany
[10]UCLouvain, Institut de Recherche Expérimentale et Clinique, MIRO Lab, Brussels, Belgium
[11]ADVACAM, Prague, Czech Republic

* Corresponding author, andrea.matamoros.ortega@sckcen.be

[†] These authors contributed equally to this work

Keywords: Proton therapy (PT), Out-of-field dose, MiniPIX Timepix detector**,** thermoluminescent detectors (TLDs), Monte Carlo (MC) simulations, TOPAS, anthropomorphic phantom.

Abstract

Objective: One major advantage of proton therapy (PT) over conventional photon radiotherapy is reduced dose delivered to normal tissue. However, the complexity of the secondary radiation field composed of a mixture of particles with a wide energy range makes its characterization a challenging task.

Approach: Measurements with a miniaturized Timepix detector were carried out in three positions out-of-field (7.4 cm, 14.1 cm, and 18.5 cm from the isocenter), inside a phantom resembling a 5 year old undergoing proton pencil beam scanning treatment for a brain tumor. Total and particle-specific deposited energy, absorbed dose, and dose equivalent in water were calculated. Results were compared with thermoluminescent detectors (TLDs) measurements and Monte Carlo (MC) simulations modelling the experimental setup.

Main results: The proton absorbed dose in water normalized to the target dose, ranged from 4.8 mGy/Gy to 65.5 μGy/Gy, while the gamma dose, which remained consistently lower, ranged between 88.4 μGy/Gy and 6.1 μGy/Gy. The measured dose equivalent varied between 6.3 mSv/Gy and 82.3 μSv/Gy. Good agreement was observed for the two farthest-locations when comparing the absorbed dose in water estimated by the MiniPIX Timepix detector with TLD measurements and MC simulations. However, the closest position showed an overestimation for both the absorbed dose and the dose equivalent, while the farthest position exhibited an underestimation for the dose equivalent.

Significance: Out-of-field dosimetry in proton therapy is challenging due to the complexity of the secondary mixed radiation field. Multiple detectors are typically required, but many are too large for use in anthropomorphic phantoms. This study demonstrates that the MiniPIX Timepix detector can accurately determine absorbed dose, dose equivalent and particle-specific contributions (electrons/gammas, protons, and ions). Unlike passive detectors such as TLDs, it enables active measurements with high time resolution, allowing dose rates analysis. The results, validated through experimental data and MC simulations, support the detector's potential for reliable out-of-field dose assessment and improved patient safety.

1 Introduction

A fundamental motivation behind the clinical implementation of proton therapy (PT) is the possible reduction of the dose delivered to normal tissues compared to conventional photon radiotherapy (RT). This is caused mainly by the physical properties of dose deposition by charged particles. The dose reduction effect of PT has been extensively investigated in comparison to various RT techniques (Busse et al., 2024; Byskov et al., 2021; Gallagher et al., 2021; Knežević et al., 2018; Newhauser et al., 2009; Newhauser & Durante, 2011; Zhang et al., 2013). As the benefits of PT were supported by many studies, the number of pediatric patients being treated with PT has increased significantly over the last decade, with the aim of reducing the risk of radiation-induced secondary effects and improving treatment outcome (Mizumoto et al., 2021; Thomas & Timmermann, 2020; Xiang et al., 2020).

Given the therapeutic benefits and the target population, it becomes imperative to understand and model the out-of-field dose in PT, which has been the subject of numerous studies over the last two decades. Many researchers have evaluated the out-of-field dose using different detection systems (Knežević et al., 2018, 2022), Monte Carlo (MC) simulations (Ardenfors et al., 2018; Newhauser et al., 2009; Taddei et al., 2009; Vedelago et al., 2022; Zacharatou Jarlskog et al., 2008) or a combination of both (Clasie et al., 2010; De Saint-Hubert, Verbeek, et al., 2022; Schneider et al., 2002; Stolarczyk et al., 2018). Furthermore, different analytical models have been developed to quantify the out-of-field dose, with the goal of simplifying dose calculation and facilitating routine clinical integration (Gallagher & Taddei, 2019; Newhauser et al., 2018; Schneider et al., 2017; Shrestha et al., 2022).

The main challenge in characterizing the secondary radiation field in PT lies in its complexity and dependency on multiple parameters. Various secondary particles of a wide energy range such as neutrons, photons, electrons, protons, light-charged particles, and heavier ions can contribute to the dose in this region. However, it is well known that neutrons are considered the main contributors

particularly in regions distant from the target. They can be generated internally by non-elastic proton interactions within the patient's body, or externally through interactions with the materials of beam-line components (Kry et al., 2017). The latter becomes less of a concern in scanning beams, which are increasingly used in modern PT facilities (Hälg & Schneider, 2020; Kry et al., 2017).

Mixed field and neutron dosimetry present a particular challenge since detectors are often only sensitive to a limited neutron energy range, and their sensitivity to different particles can impact the interpretation of the detector's response. The complexity is further compounded when measuring in-phantom, as the neutron energy spectrum is highly dependent on the target geometry (Baiocco et al., 2016). Using a combination of dosimetry systems, each with a specific and known response to particle type and energy range, can provide a more comprehensive and detailed assessment of the radiation field, making it a useful approach (De Saint-Hubert, Verbeek, et al., 2022; Knežević et al., 2022; Stolarczyk et al., 2018). However, this approach can be time-consuming and requires a complex setup and multiple irradiations with potentially large doses delivered to the target. Alternatively, MC simulations are considered a valuable and flexible tool for such applications, allowing for a more detailed analysis of the radiation field. Nevertheless, simulation results can be influenced by the choice of MC code and the implemented physics models (Colson et al., 2024; De Saint-Hubert, Farah, et al., 2022; Lai et al., 2025; Vedelago et al., 2022).

Timepix-based detectors are versatile for applications that require high-resolution spectral and spatial information, particularly in radiotherapy (Rosenfeld et al., 2020). They have been extensively used for the characterization of proton and heavy ion beams (Bisogni et al., 2009; Gehrke et al., 2017; Granja et al., 2011; Gwosch et al., 2013; Reinhart et al., 2017; Stasica et al., 2020) as well as mixed radiation fields (Granja, Jakubek, et al., 2018; Jakubek et al., 2010; Oancea, Granja, et al., 2023; Opalka et al., 2012, 2013). Single-event detection along with high-resolution pattern recognition algorithms allow different particle types to be resolved, along with their energy loss, linear energy transfer (LET), and trajectory (Granja et al., 2021, 2022). This makes Timepix detectors ideal for mixed-field characterization. Moreover, the miniaturized MiniPIX Timepix detector offers a significant advantage due to its size for conducting measurements inside phantoms (Granja, Kudela, et al., 2018).

The majority of these studies were performed with Timepix detectors equipped with silicon sensors. For medical applications, it is worth converting dosimetric quantities in silicon to water or tissue-equivalent materials, which are more clinically relevant. The use of an anthropomorphic phantom offers a more realistic scenario for dosimetric evaluations and supports the potential application of the results in future clinical treatments for radioprotection concerns. To the knowledge of the authors, most of the previous studies have focused on LET determination, often using simplified or non-anthropomorphic phantoms. Although, some of these studies included MC simulations, to the author's knowledge, none have included comparisons with TLD detectors, which are well-established tools for measuring secondary radiation fields.

The aim of this study is to demonstrate the utility of the compact MiniPIX Timepix detector for characterizing the mixed secondary radiation field in PT through measurements inside an anthropomorphic phantom, which resembles a 5 year old typical in size, weight and shape,

receiving a proton pencil beam scanning (PBS) treatment for a brain tumor. Additionally, a new acquisition method is tested to address detector dead time and prevent particle mischaracterization. The total and particle-specific deposited energy, dose rate, absorbed dose, and dose equivalent in water are calculated. The results are benchmarked against measurements with thermoluminescent detectors (TLDs) and MC simulations. This study is motivated by the need for advanced technologies, such as the Timepix detector, and methodologies, that can support the proton therapy community in accurately characterizing out-of-field doses. A better understanding of these secondary doses and how they are influenced by the selected clinical treatment parameters, can contribute to the development of radiation protection guidelines, particularly for radiosensitive populations such as pediatric patients, ultimately preventing radiation induced secondary malignancies.

This article is part of Racell Nabha's PhD thesis (Nabha, 2023). The measurements were repeated using a new acquisition methodology, and the results are reported here.

2 Materials and Methods

2.1 Experimental set-up

A pediatric anthropomorphic phantom (ATOM, Type 705D, Computerized Imaging Reference Systems (CIRS), Inc., Norfolk, VA, USA) was used in this study. The phantom resembles a reference 5 year old child, it is 110 cm tall and weighs 19 kg. It consists of 26 slices (each 25 mm thick) made of tissue-equivalent material and contains 180 detector holes in various organ positions.

A clinical proton treatment plan delivered to a 7-year-old female patient with diffuse midline glioma was adapted to this study. The cranium of the selected pediatric patient resembled that of the anthropomorphic phantom in terms of size and shape. The treatment plan comprised three fields, as described in Table 1 and shown schematically in Figure 1, all of which included the use of a range shifter. The fields were delivered to a 195 cm^3 planning target volume (PTV) with a total prescribed dose of 5 Gy (RBE) to the target. The dose per field was 1.70 Gy, 1.64 Gy, and 1.63 Gy for fields 1, 2 and 3, respectively. Irradiations were carried out at the West German Proton Therapy Centre Essen (WPE, Essen, Germany), using the PBS implementation of the Proteus®PLUS PT system (IBA, Louvain-La-Neuve, Belgium). The treatment plan was created using the treatment planning system (TPS) RayStation version 7 (RaySearch Laboratories, Stockholm, Sweden) and the MC-based dose engine (version 4.1) of RayStation for planning dose distributions. A computed tomography (CT) scan of the phantom was performed and registered with the clinical CT and the RT structures, including the target volumes and organs-at-risk (OARs). The phantom was placed in supine position on the treatment couch and aligned with the lasers of the positioning system (Figure 2).

	Field 1	Field 2	Field 3
Gantry angle (°)	260	110	70
Couch angle (°)	15	345	0
Number of energy layers	27	24	26
Min-max beam energy (MeV)	100-167	100-159	100-166

Table 1: Overview of the parameters of the three fields used in the treatment plan for the current study

Various dosimetry systems were used for measuring the out-of-field dose inside the phantom, namely different types of TLDs, bubble detectors for personal neutron dosimetry (BD-PNDs), and the MiniPIX Timepix detector. Measurements with the first two types of detectors were described in detail elsewhere (De Saint-Hubert et al., 2022 b). TLDs in the form of cylindrical chips (4.5 mm diameter, 0.9 mm height) type MTS-7 (^{7}Li-enriched LiF: Mg, Ti), which are mostly sensitive to photons, electrons, protons, and heavier ions, were placed in various organ positions out-of-field. Their distances from the isocenter ranged between 7 cm and 50 cm. The absorbed doses measured by MTS-7, reported as absorbed dose in water per target dose (μGy/Gy), were included in this study for comparison with the MiniPIX Timepix detector presented in section 2.3.

2.2 Monte Carlo simulations

While we refer to De Saint-Hubert et al. (2022b) for a comprehensive description of the simulation framework, a brief overview is provided below along with relevant findings for comparison and validation of doses measured by the MiniPIX Timepix detector.

A DICOM-based dose verification system for simulating the out-of-field absorbed dose was carried out using TOPAS v3.6 (Faddegon et al., 2020; Perl et al., 2012) in combination with the matRad toolkit v2.10.1 (Wieser et al., 2017) written in Matlab (The Mathworks, Inc., Natick, MA, USA). TOPAS simulations were designed to reproduce the commissioned beam (Bäumer et al., 2015), specifically the measured depth dose curves by adjusting the mean energy and spread from the lowest to the highest available energies (Bortfeld, 1997; Clasie et al., 2012; Grassberger et al., 2014). The proton pencil beams were also fully characterized using the Fermi-Eyges parameters from the beam model based on measurements at WPE (Verbeek et al., 2021). The number of proton histories in the simulations was calculated following a calibration of Monitor Units (MU) to ions. The TOPAS physics modules used in the simulations based on Geant4 physics models (Jarlskog & Paganetti, 2008) were the following: g4em-standard_opt4, g4h-phy_QGSP_BIC_HP, g4decay, g4ion-binarycascade, g4h-elastic_HP, and g4stopping.

The DICOM CT images of the phantom were imported into TOPAS with a grid size of 0.2 x 0.2 x 0.2 cm³, which is consistent with the grid size used in RayStation. The TOPAS and matRad framework were validated through a 3D gamma test by comparing the scored absorbed dose to water with the RayStation simulation results. A gamma pass rate of 99.3% was produced for a global 3D gamma test with passing criteria of 1% and 2 mm.

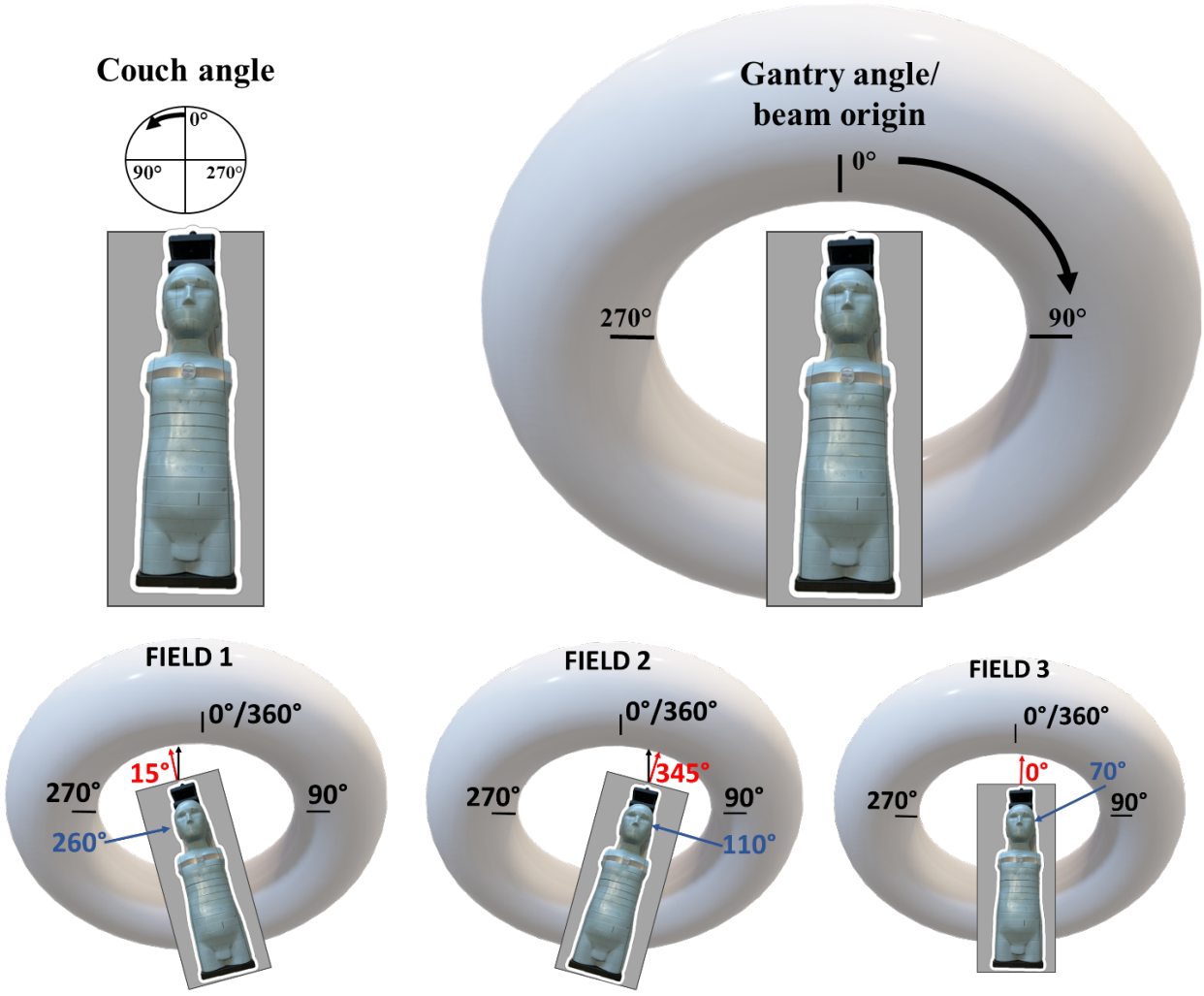

Figure 1: Schematic representation of the beam direction towards the anthropomorphic phantom for each field considered. The machine's angular configuration is shown for the couch angle (top left) and gantry angle (top right). The bottom figures illustrate the beam directionality for each field, highlighting the selected gantry angle (blue arrows), which also indicates the beam's origin, and the couch angle (red arrows).

Since the secondary neutron production and, hence, the out-of-field dose are dependent on the materials inside the gantry treatment room (Englbrecht et al., 2021), an elaborate room model was included in the simulations. The simulation geometries included the following: a gantry structure oriented around the isocenter featuring an aluminum rolling floor, iron focusing and bending magnets, an iron counterweight, a Kevlar patient table and its mount made of aluminum and iron, a gantry pit, and concrete maze, ceiling, floor, and room walls. To calculate the out-of-field dose, 10^{10} primary proton histories were used. The simulation physics models were set identically to those used in the MU/ion calibration described earlier.

The total dose equivalent was calculated by summing the contributions from primary protons (relative biological effectiveness, RBE=1.1), secondary gamma rays (RBE=1), and neutrons. For

neutrons, the dose equivalent at a reference point in the radiation field was determined using fluence-to-neutron dose equivalent conversion factors calculated as the product of tissue kerma factors and energy dependent radiation quality factors from literature as was done in (Romero-Expósito et al., 2016).

2.3 MiniPIX Timepix detector

The MiniPIX Timepix detector developed by ADVACAM (Prague, Czech Republic) is a hybrid semiconductor pixel detector consisting of a silicon sensor bump-bonded to a pixelated readout ASIC (Application-Specific Integrated Circuit) Timepix chip. The chip features a high-granularity 256 × 256 pixel matrix with a 55 µm pixel pitch and a total sensitive area of 14.08 mm × 14.08 mm (Granja, Kudela, et al., 2018). The detector used in this work is equipped with a 500 µm thick Si sensor and a Timepix chip. A bias voltage of 80 V was chosen to obtain a nearly fully depleted sensor, which enhances the charge sharing effect and mitigates high energy saturation in the pixels (Campbell et al., 2008; Granja et al., 2011). Consequently, the depletion thickness of the sensor was slightly reduced to 475 µm as demonstrated in another work (Nabha et al., 2022).

Each pixel can be configured to operate in one of the three modes: counting, Time-of-Arrival and Time-over-Threshold (ToT), also known as energy mode (Llopart et al., 2007). In this study, the detector operated in both counting and energy mode. The counting mode enables measurements of the number of particles that hit each pixel with an energy deposition exceeding the threshold (Granja, Jakubek, et al., 2018), while the energy mode allows the measurement of the total deposited energy at the pixel level through an energy calibration process (Jakubek, 2011). A more detailed description of the acquisition method is provided in Section 2.4.

The MiniPIX Timepix detector was inserted into three different slices of the phantom (slice number 8, 11 and 13), on the front side with the sensitive volume facing the cranium. To this end, the original slices of phantom were replaced by three customized polymethyl methacrylate (PMMA) slices of the same dimensions, which included inserts designed to hold the detector (Figure 2). The three measurement positions were located at 7.4 cm (position 1), 14.1 cm (position 2) and 18.5 cm (position 3) from the isocenter, measured up to the center of the sensitive volume of the detector. The distance to the PTV ranged between 3.4 cm and 15.9 cm. The detector was connected via USB cable to a PC and was controlled and operated using the PIXet Pro software package version 1.8.1 (*PIXet - ADVACAM Wiki*, n.d.), which enabled parameter control, data acquisition and online visualization of the radiation field.

2.4 MiniPIX Timepix data acquisition

The MiniPIX Timepix detector captures data in a frame-based mode, where each frame is acquired over a user-specified time, with a minimum acquisition time of 0.3 ms. After each frame is acquired, the detector undergoes a dead time of approximately 20 ms (Granja, Kudela, et al., 2018). Selecting an appropriate acquisition time is crucial to ensure accurate tracking of individual particles and limit event overlap. If the acquisition window is too wide, overlaps between clusters can hinder proper particle identification and potentially saturate the detector's pixels. Conversely, using short acquisition times, such as the minimum 0.3 ms, can prevent these issues but will result in a large dead time relative to the acquisition time. Total dose assessment, in this case, comes with

significant uncertainties if the radiation field varies over time, due to the need for interpolation between the frames to estimate the dose accumulated during the dead time. The previous considerations prompted us to test a new acquisition method, incorporating both short and long acquisition times. Short acquisition provides the best data for particle identification, while long acquisition provides the best data for assessing the total energy deposited.

To define the acquisition times for both short and long acquisitions in energy mode, preliminary measurements in count mode were conducted. The detector was positioned in the three different positions and irradiated six times using various acquisition times: 0.3 ms, 0.5 ms, 0.8 ms, 100 ms, 200 ms and 500 ms. The first three were considered for short acquisitions and the last three were considered for long acquisitions. Only field 2 was used for these measurements, as it was observed in a previous experiment to exhibit a high dose rate at various out-of-field locations. To select appropriate acquisition times for short acquisitions, a graphical analysis of the acquired frames was performed using the PIXet GUI. The criterion was to minimize the presence of overlaps and overloaded areas where clusters could not be properly characterized per particle. If excessive overlaps were observed, the acquisition time was reduced.

For long acquisitions, each frame is highly populated with events, meaning that most pixels are hit by more than one particle. To prevent pixel saturation, the detector developer suggested to keep the number of hits per pixel in a frame below 1000. It was observed that even the longest acquisition time tested would comply with this criterion for position 1, which is the nearest to the treatment region. Since farther positions experience fewer events, a longer acquisition time was considered appropriate. Consequently, we performed measurements using an acquisition time four times longer than the tested one, which resulted into a successful acquisition.

Table 2 presents the selected acquisition times for the energy mode measurements.

Position / Distance from isocenter (cm)	Selected acquisition time (ms)	
	Short acquisitions	Long acquisitions
P1 / 7.4	0.3	500
P2 / 14.1	0.8	2000
P3 / 18.5	1.0	2000

Table 2: Selected acquisition times for energy mode measurements with the MiniPIX Timepix detector at the different out-of-field positions.

Once the acquisition times were defined, energy mode measurements were conducted using the MiniPIX Timepix detector. These were performed separately for the three different fields at each of the three positions. To improve statistical accuracy, short acquisitions were repeated multiple times, while long acquisitions were performed only once.

2.5 MiniPIX Timepix data analysis

2.5.1 Data pre-processing of short acquisition time measurements

Pixel clusters, also known as particle tracks, play a fundamental role in the analysis of Timepix data. They are formed when a particle deposits energy in the sensor, followed by a diffusion of the liberated charge resulting in the spread of the signal to adjacent pixels (Campbell et al., 2008). By

analyzing the track and morphology of each cluster, several physical parameters can be obtained and further used to discriminate between different particles. This is mainly useful in mixed radiation fields such as the ones encountered in this work. The analysis of the data for the short acquisition time measurements consisted of a two-step process. First, pre-processing of the data was carried out using the Data Processing Engine (DPE), which is a tool developed by ADVACAM for processing the data acquired with Timepix detectors (Marek et al., 2024). Using the Clusterer software implemented within the DPE, the pixelated data were converted into cluster lists characterized by several parameters (Oancea, Granja, et al., 2023). These features can be broadly grouped into spectral, morphological and tracking information (Granja et al., 2021).

In addition to the cluster lists, the particle identification feature of the DPE based on dense neural networks was also selected. The particle classification for each event was performed based on the following three classes: 1) photons and electrons, 2) protons, and 3) heavier ions. Therefore, the output of this step was an exhaustive cluster list with several parameters characterizing each cluster including predicted particle class.

2.5.2 Data processing for short acquisition time measurements

The absorbed dose rate in silicon per frame was calculated using the equations below:

$$DR = \frac{D}{t_{fr}} \tag{1}$$

$$D = \frac{\sum_{i=1}^{N} depE_i}{M} \tag{2}$$

Where equation 1 defines the measured dose rate in silicon, *DR* (Gy/h), with D being the absorbed dose in silicon (Gy), and t_{fr} is the frame acquisition time (h). Equation 2 describes the absorbed dose D, where *i* is the cluster or event number, $depE_i$ is the deposited energy of event *i* (keV), *M* is the mass of the sensitive volume (kg),and *N* is the total number of events per frame. This calculation was applied to all the particles and to each of the three particle classes described above, separately. As such, *N* was considered as the total or the particle-specific number of events.

Since silicon is not equivalent to water or tissue, the absorbed dose measured by the MiniPIX Timepix detector was converted into absorbed dose in water. The conversion method involves correlating the LET in silicon calculated per cluster by the DPE with the silicon electronic stopping power from the NIST database to define a conversion coefficient, which is the ratio between the stopping power of water and silicon (Parisi et al., 2022). In the case of protons, the LET was first corrected for protons stopping within the sensor, following the method described in previous work (Nabha et al., 2023).

The conversion method utilized the NIST tables for stopping power in both silicon and water, specific to each particle type: ESTAR, PSTAR and ASTAR (Berger et al., 1999a). For photons and electrons, the ESTAR database was used, as electrons are the primary interacting particles with the sensor. For protons, the PSTAR database was employed. Finally, for ions, TOPAS simulations

provided information on the different types of ions interacting with the detector in out-of-field positions, where alpha particles were found to be the predominant ions. The ASTAR database was used for alpha particles.

The conversion coefficients were then multiplied by the energy deposited in silicon to calculate the deposited dose in water. This dose is not reported within the results. The same conversion coefficients were applied to the LET in silicon to obtain the LET in water, which is necessary for the subsequent calculations.

Lastly, the quality factor Q was calculated. The LET-dependent Q factor is used to characterize the biological effectiveness of a radiation quality.

A Q value of 1 was assigned to electrons and photons. For protons and heavier ions, Q was calculated based on their LET in water (Yonekura et al., 2014):

$$\begin{aligned} Q &= 1 && LET_w < 10\ \frac{keV}{\mu m} \\ Q &= 0.32 \times LET_w - 2.2 && 10 \leq LET_w < 100\ \frac{keV}{\mu m} \\ Q &= \frac{300}{\sqrt{LET_w}} && LET_w > 100\ \frac{keV}{\mu m} \end{aligned} \quad (3)$$

2.5.3 Data processing for long acquisition time measurements

Long acquisitions allow to limit the dead time; however, due to the overlap between events, particle characterization is not possible. As a result, the DPE is not suitable for these types of measurements. Instead, to obtain the energy deposited, a direct conversion between ToT signal and energy was performed, this conversion follows the calibration function described by Jakubek et al (2011). The absorbed dose in silicon was then calculated by Equation (2).

To convert the absorbed dose in silicon to absorbed dose in water D_w, the average conversion coefficient derived from all short acquisitions for a particular position and field was used. To calculate the dose equivalent H (mSv), the absorbed dose in water was multiplied by the average quality factor Q, as defined in (Yonekura et al., 2014):

$$H = D_w \times Q(LET_w) \quad (4)$$

A correction for the dead-time was carried out in the following way. The average dose rate between two consecutive frames for the different quantities (dose in silicon, dose in water and dose equivalent) was calculated and multiplied by the dead time between frames. These values were then added to the respective totals for each quantity. This step was essential for the comparison with the doses obtained from TLD measurements and MC simulations.

Finally, the dose per particle was determined by applying a relative weighting according to the short measurements.

To estimate the overall measurement uncertainty of the absorbed dose in water and dose equivalent, different contributing factors were considered. These uncertainty analysis included the energy resolution of the Timepix chip, reported to range between 5-8% (Sommer et al., 2022); the uncertainty in particle classification from the DPE, estimated at approximately 3% (Marek et al., 2024); uncertainties in the stopping power values extracted from the NIST database, estimated to be 2-3% for electrons and 5-10% for protons and alpha particles; and a positioning uncertainty of approximately ~2 mm, which based on MC data can range between 10% to 25% on the absorbed dose, depending on the dose gradient in the measurement location. The average for each contribution was calculated and then combined in quadrature, resulting in a total uncertainty of approximately 20% for the absorbed dose in water, which also applies to the dose equivalent. A diagram illustrating the data processing for both short and long acquisition time measurements is presented in Figure 3.

3 Results

3.1 Particle identification and deposited energy spectra

Figure 2 displays representative frames captured by the MiniPIX Timepix measurements in each of the three slices of the phantom. Specifically, the frames correspond to all the fields (rows) for all the positions (columns). Measurements in position 1 revealed a nearly homogenous field, dominated by protons with a preferential direction and predominantly elevation angles greater than 60 degrees. However, farther from the target this was no longer the case, as a mixed radiation field with decreased fluence became prevalent, and the elevation angles for protons became smaller. Figure 4 illustrates the number of identified particles and the various proton elevation angles for a short measurement at position 1 and position 3, confirming the earlier observations.

A relationship was observed between the directionality of the tracks formed in the acquisition frames and the specific beam direction configuration for each field. Combined, Figures 1 and 2 help to illustrate this relationship more precisely. For example, in field 1, the gantry is tilted to 260 degrees and the couch is tilted to 15 degrees, indicating that the beam is expected to impinge diagonally on the right side of the head of the phantom (viewed from top to bottom) (Figure 1, bottom left). In Figure 2, the event tracks recorded by the MiniPIX Timepix detector exhibit a diagonal pattern moving from right to left in the sensor region. Similar behavior is observed for the other fields.

Figure 5 presents the fluence energy distribution per unit lethargy in terms of deposited energy in silicon corresponding to all particle types and the three separate classes of events at the three phantom positions for a short acquisition. The lethargy u is defined as:

$$u = ln\left(\frac{E_{j,upper}}{E_{j,lower}}\right) \quad (5)$$

Where $E_{j,upper}$ and $E_{j,lower}$ are the upper and lower energy boundaries of energy bin j, respectively. The fluence per lethargy is then determined by dividing the fluence in each energy bin j by the lethargy.

In this context, the term energy refers strictly to the energy deposited by the particles.

This representation per unit lethargy is commonly used for neutron spectra due to their wide range of energies and allows for direct comparison of the area under one portion of the curve to the area under another portion when using a logarithmic energy axis. The results show that the fluence energy distributions varied depending on the type of particle and measurement position. Three important peaks can be observed, the first two centered around 30 keV and 170 keV, which correspond to photons and a third peak for protons. The latter exhibited a broad distribution centered at around 1.8 MeV and 2.1 MeV in positions 1 and 3, respectively. The spectra also show that the contribution of protons is the highest particularly in position 1, while the relative contribution of photons increases with increasing distance from the isocenter. The fluence energy distribution by heavier ions remained almost unchanged and very low with respect to photons and protons across all positions.

3.2 Particle contribution to absorbed dose in silicon

Table 3 presents the particle contributions to the total absorbed dose per average dose per field in silicon with dead time correction across different fields and positions. This information elucidates the influence of the field characteristics (described in Table 1) on dose deposition. It can be observed that protons are the primary contributors to the total dose in all positions and fields. Field 2 exhibits the highest total dose at position 1, yet it records the lowest total dose at more distant positions. This behavior can be attributed to the dominance of low-energy secondary protons in this field, which deposit most of their energy near the source but lack sufficient energy to reach out-of-field positions, such as position 3 (P3). This is further supported by the increase in gamma contributions, which rise from 1.6% in P1 to 20% in P3 for field 2. The ion contribution remains relatively consistent across fields at all positions.

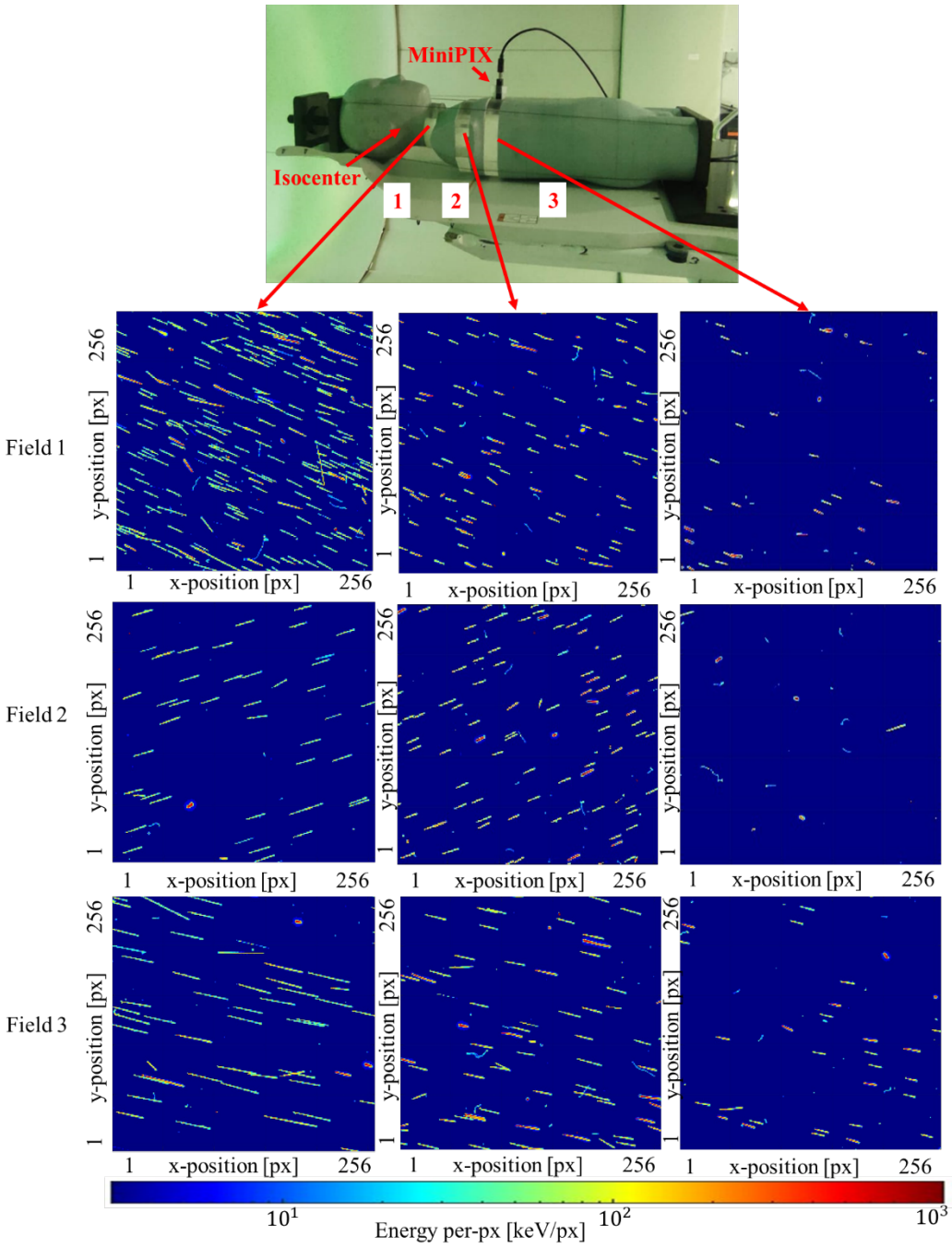

Figure 2: Top: Anthropomorphic phantom (5-year-old ATOM, CIRS) in supine position with MiniPIX Timepix detector inserted in position 3. Bottom: Representative Timepix frames obtained from measurements in the three positions located at 7.4 cm (position 1), 14.1 cm (position 2) and 18.5 cm (position 3) from the isocenter and for the three different fields used. The tracks observed within the detection system represent different particles impinging it, which then are classified in photons/electrons, protons and ions by considering their characteristics, i.e., linearity, roundness, etc. Identified particles based on this track analysis are shown within the frames. Color bars show the deposited energy per pixel.

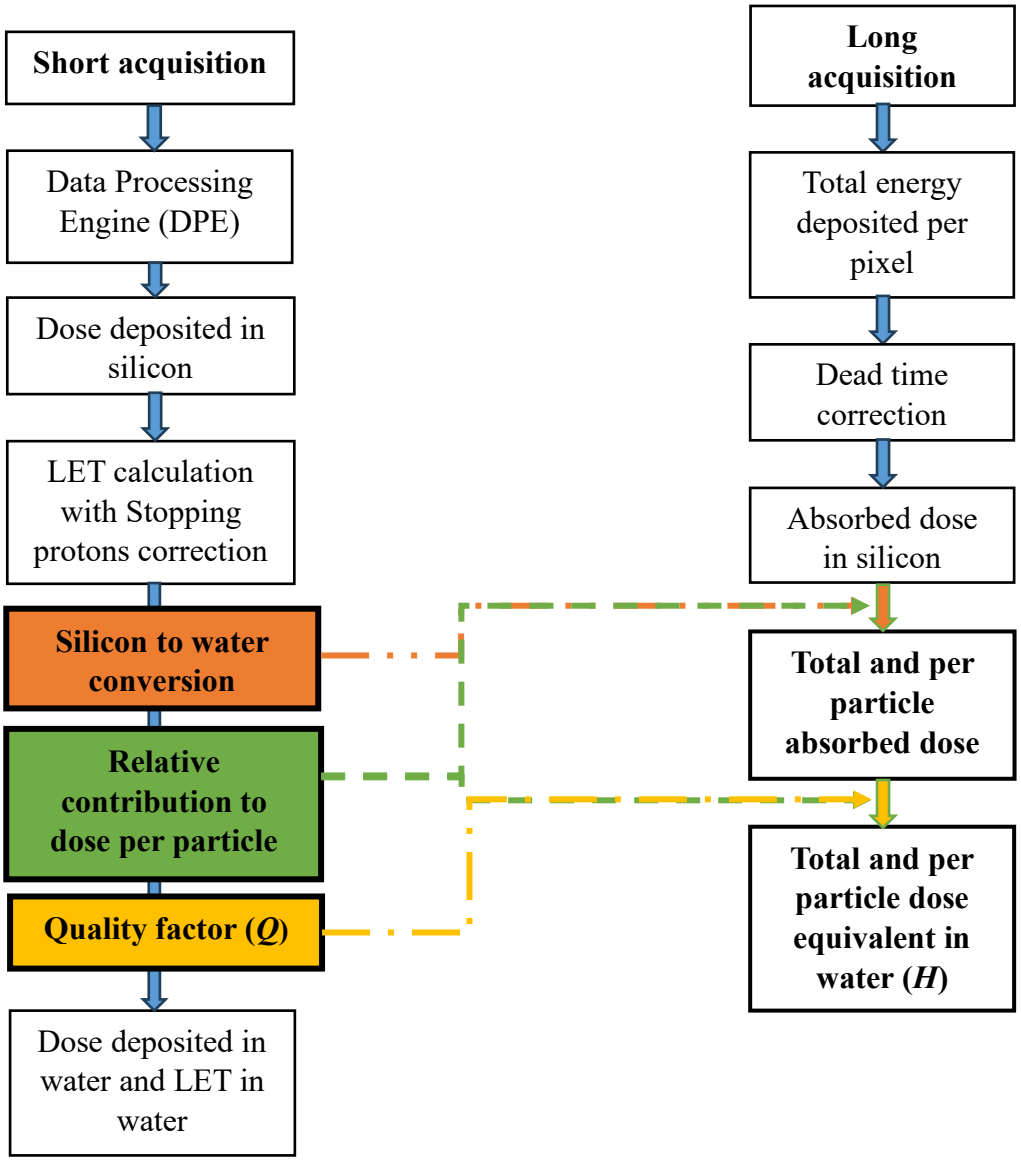

Figure 3: Data processing diagram for both short and long acquisition times measurements.

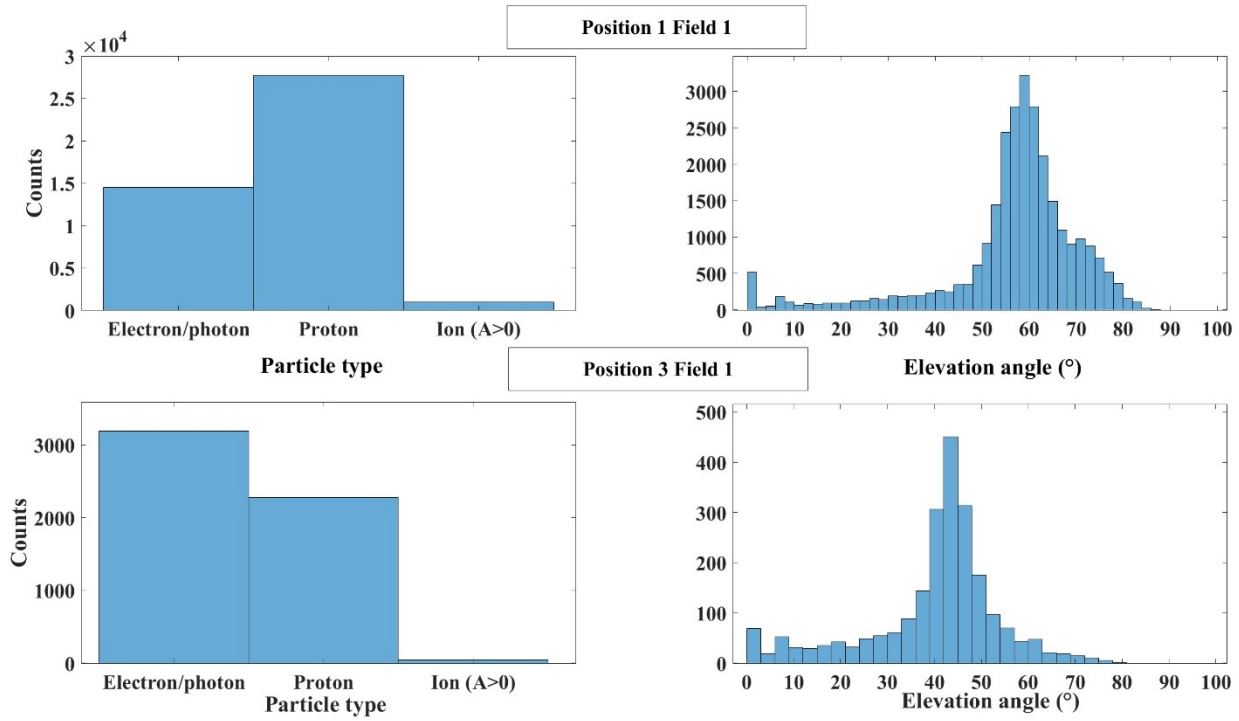

462 *Figure 4: Particle identification and proton elevation angles for field 1 at position 1 (top) and position 3 (bottom).*

463

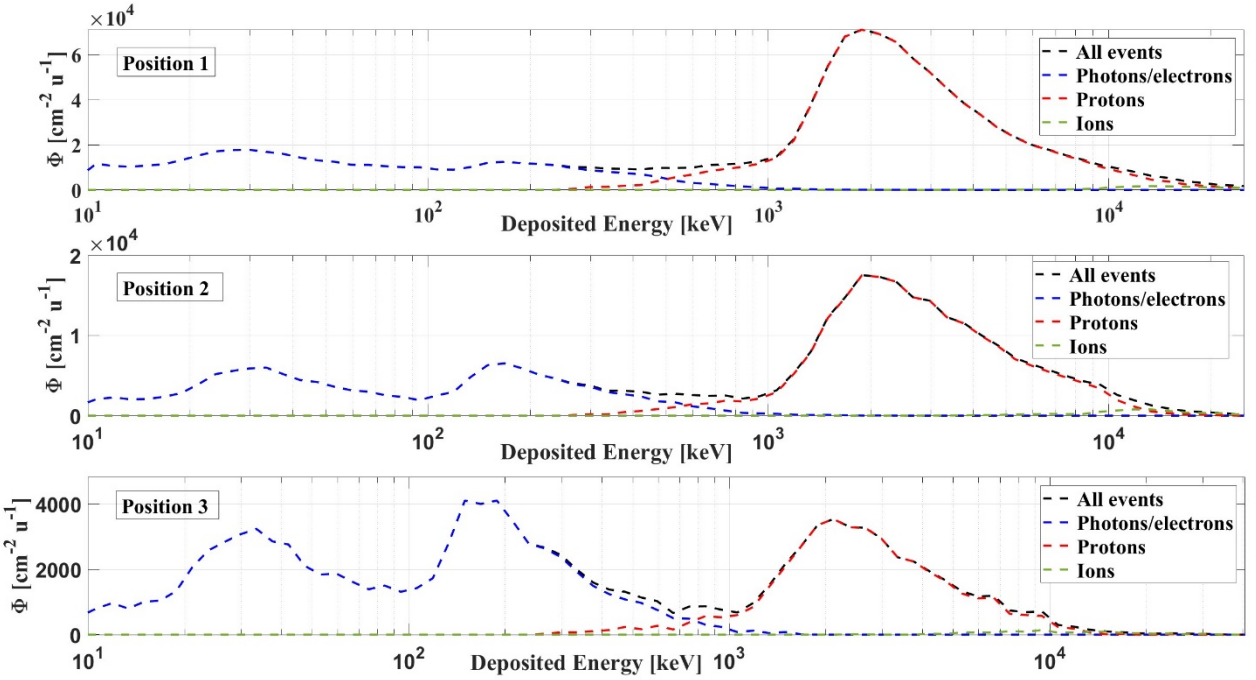

Figure 5: Fluence energy spectra per unit lethargy in terms of deposited energy in silicon obtained from MiniPIX Timepix short measurements in position 1 (top), position 2 (middle) and position 3 (bottom) inside the phantom. Dashed black, blue, orange and green lines represent the contributions of all events, photons/electrons, protons and heavier ions, respectively.

Position	Field	Absorbed dose in silicon per average dose per field (µGy/Gy) - % contribution to total			
		Photon/Electron	Proton	Ion	Total
P1	F1	87.55 (2%)	3993.97 (92.4%)	241.22 (5.6%)	4322.74
	F2	85.72 (1.6%)	4752.27 (88.1%)	558.52 (10.3%)	5396.51
	F3	48.86 (1.0%)	2881.19 (60.1%)	1860.75 (38.8%)	4790.80
P2	F1	9.90 (2.5%)	348.57 (89.5%)	30.99 (8.0%)	389.46
	F2	9.52 (3.6%)	254.48 (96.1%)	22.8 (8%)	286.8
	F3	9.85 (1.8%)	450.93 (83.3%)	80.51 (14.9%)	541.29
P3	F1	5.11 (6.6%)	67.42 (86.7%)	5.24 (6.7%)	77.78
	F2	4.70 (20.4%)	15.09 (65.5%)	3.22 (14.0%)	23.01
	F3	5.40 (6.4%)	72.88 (86.5%)	5.94 (7.1%)	84.22

Table 3: Deposited dose in silicon per target dose contribution by particles within the different frames and positions measured with Timepix detector. The percentage contribution of each particle type (photons/electrons, protons and ions) to the total dose is shown below each quantity. Field 2 in position 1 and 3 is highlighted, as it demonstrates a notable contribution from low energy secondary protons which deposits their energy close to the field. In the furthest position, this is reflected in the increase of photons/electrons dose contribution.

3.3 Dose rate as a function of time

The variation of the total and particle-specific dose rate with time for position 2 and position 3 is illustrated in Figure 6. The results shown represent the dose rate in silicon without applying dead time correction. Several observations can be made from these results. Firstly, the maximum dose rate observed of 3.5 Gy/h in position 2 dropped to 0.4 Gy/h in position 3. Protons were identified as the major contributors to the dose rates across all positions and fields, with a pronounced variation in proton dose rates over time, while photon dose rates remained nearly constant.

Within the two positions the total dose rate was found to decrease with time, which can be attributed to the fact that during PBS, the dose is delivered in iso-energy layers starting from the highest energy or the most distal layer to the lowest energy layer. Consequently, the higher energy layers contribute more to the out-of-field dose observed at these two positions.

The plots also reveal column-like structures, which offer insights into the time structure of the detector during a field irradiation. Meaning that the column-like structures can be related to the PBS energy layers delivered. In the case of position 2 field 1, 24 column-like structures are visible, which is fewer than the 27 expected for this field. This discrepancy can be attributed to the chosen

acquisition time, being 25 times shorter than the theoretical dead time of approximately 20 ms. This mismatch likely caused the detector to miss some energy layers.

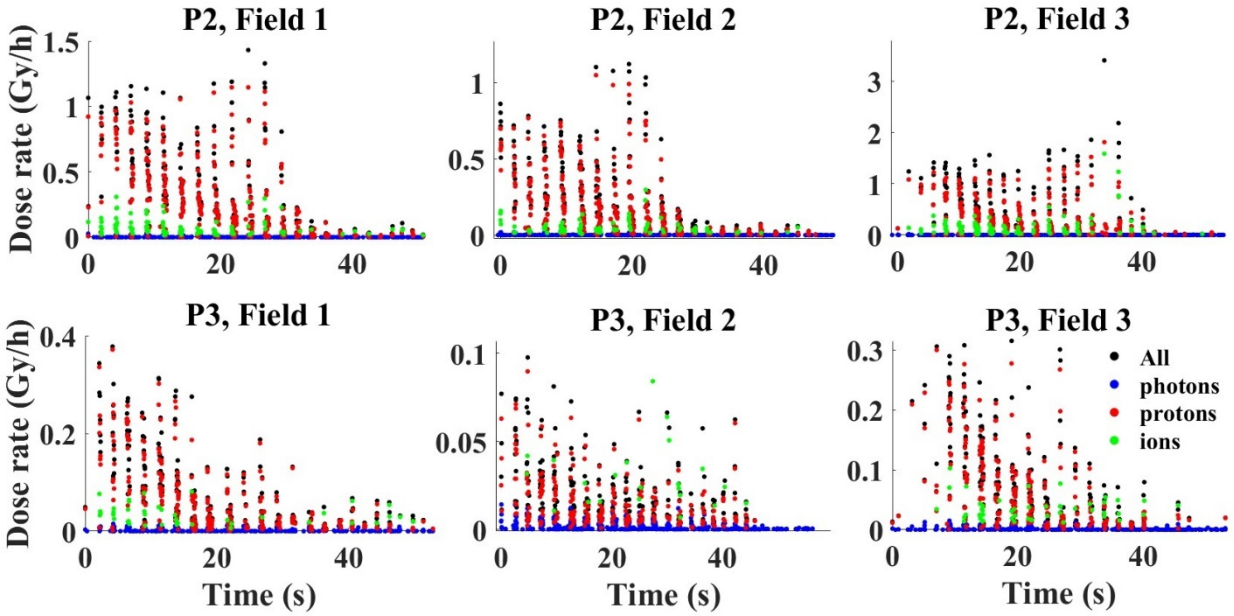

Figure 6: Measured dose rate in silicon as function of time by all particles (black), protons (red), heavier ions(green) and photons/electrons (blue). The plots are displayed for positions 2 (top), and 3 (bottom), and for fields 1 (left), 2 (center) and 3 (right). The dose rates were calculated based on the sum of the deposited energy per frame, with a frame acquisition time specific for each position (table 2). No dead-time corrections were applied.

3.4 Absorbed dose and dose equivalent in water

Figure 7 displays the absorbed dose in water and the dose equivalent as a function of the distance from the isocenter, obtained from MiniPIX Timepix measurements and compared with TOPAS simulations and TLD measurements. The reported values for the MiniPIX Timepix detector include the correction for dead-time. They are as well presented with an estimated total uncertainty of approximately 20%. This estimate accounts for several contributing factors: the energy resolution of the Timepix chip reported to range between 5% and 8% (Sommer et al., 2022); the particle identification uncertainty from the DPE estimated at 3% (Marek et al., 2024); uncertainties in the stopping powers obtained from the NIST tables, which range between 2% to 3% for electrons and 5% to 10% for protons and alpha particles (Berger et al., 1999b); and positioning uncertainty estimated between 10% and 25%. Further details regarding these uncertainties are discussed in the discussion section.

The comparison between MiniPIX Timepix and TOPAS (Figure 7, top) revealed a good agreement for both proton and gamma absorbed doses in water for positions 2 and 3, whereas position 1 results from MiniPIX Timepix were significantly higher than the TOPAS simulations by a factor of 2.53 for protons and 4.79 for gammas. Specifically, the MiniPIX Timepix results indicated that the proton dose varied from 4.8 mGy/Gy at position 1 to 65.5 µGy/Gy at position 3. The percentage difference between the Timepix-measured and simulated proton doses were 153% for position 1,

27% for position 2 and -17% for position 3. In contrast, the gamma dose was consistently lower than the proton dose, ranging from 88.4 µGy/Gy at position 1 and 6.1 µGy/Gy at position 3. The percentage differences between the measured and simulated gamma doses were 379%, 24% and 7% for positions 1, 2 and 3, respectively.

The total absorbed dose in water and the sum of proton and gamma doses measured by the MiniPIX Timepix were also plotted against the sum of simulated proton and gamma doses and TLD measurements (Figure 7, middle). The total MiniPIX Timepix measured absorbed dose ranged between 6.1 mGy/Gy and 77.8 µGy/Gy. Measurements showed that the contribution of heavier ions to the total absorbed dose in water was 18% , 9% and 7% for positions 1, 2 and 3, respectively.

Finally, the total dose equivalent estimated from MiniPIX Timepix measurements and simulations is presented in Figure 7 (bottom), ranging from 6.3 mSv/Gy and 82.3 µSv/Gy. This one was compared to TOPAS simulations, where contributions from protons, gammas and neutrons are included. A good agreement was observed at position 2 with a percentual difference of -19% between measurements and TOPAS. An overestimation by a factor of 2 was evident for position 1, whereas an underestimation by a factor of 0.3 was noted for position 3.

4 Discussion

This study evaluated the capabilities of the silicon-based MiniPIX Timepix detector in characterizing the mixed radiation field present at out-of-field locations during a PT treatment. A method was tested to calculate dosimetric variables, including absorbed dose in water and dose equivalent, with results compared to MC simulations and TLDs measurements. The latter presented a good agreement with respect to absorbed dose in water for positions located farther away from the isocenter. However, the dose equivalent exhibited good agreement only at the middle out-of-field location, while it was overestimated at the closest position and underestimated at the farthest position.

Additionally, a new acquisition method was introduced to prevent particle mischaracterization and overcome the detector dead time. The strategy involved in performing two types of measurements: short acquisitions, optimized for particle characterization by reducing the likelihood of event overlap; and long acquisitions, used to improve dose evaluation and minimize the impact of dead time. This approach is innovative as previous studies typically relied on single measurements often neglecting dead time corrections, which leads to a data loss within measurements. This method allowed us to obtain results for both total and particle specific absorbed dose, which were comparable to previous experimental and simulation results.

The MiniPIX Timepix detector provided detailed, event-specific information for our irradiations. This allowed us to characterize the absorbed dose for each field considered, and to observe the influence of the treatment plan's angular configuration (selected gantry and couch angles) of each field on proton interactions. These interactions, in turn, impact the generation of out-of-field doses. In our study, the angular configuration of field 2 contributed primarily to the total dose in water at positions near the isocenter, with a contribution of 37%, which decreased to 12% at more distant positions. This reduction was attributed to the protons generated with this angular configuration

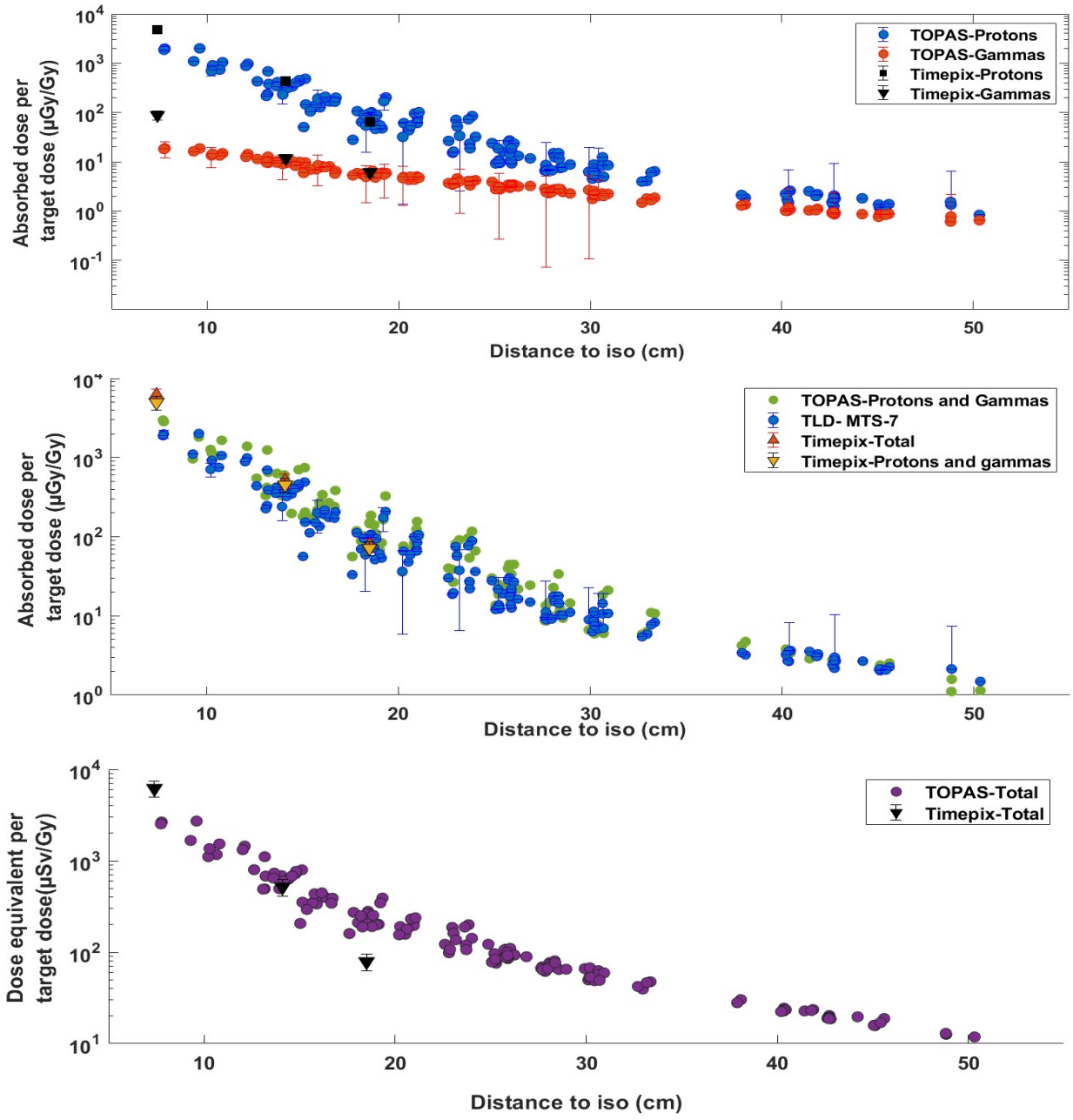

Figure 7: Top: Absorbed dose in water from simulations for protons (orange circles) and gammas (blue circles) and Timepix measurements for protons (black squares) and gammas (black downward triangles). Middle: Sum of simulated proton and gamma absorbed doses in water (green circles), measured TLD type MTS-7 absorbed doses in water (blue circles), total MiniPIX Timepix absorbed doses in water (black upward triangle) and sum of Timepix proton and gamma absorbed doses in water (orange downward triangle). Bottom: Total dose equivalent estimated from TOPAS simulations (purple circles) and MiniPIX Timepix measurements (black upward triangle). To ensure readability, error bars representing (k=1) for TOPAS and TLD results are displayed for every 10th data point. All the values were normalized to the physical target dose (Gy) and the plots were adapted from the work of De Saint-Hubert et al 2022b

depositing most of their energy in positions near the isocenter. As these protons lose energy, they are unable to reach farther positions and instead interact, increasing the gamma dose contribution. Delving deeper into the influence of the angular configuration and beam direction towards the phantom, it is important to note that field 2 has a similar angular configuration to field 1, forming an almost a mirrored setup. The important difference is that the gantry angle of field 2 is inclined 10 degrees higher than field 1. Such analyses help us to understand the out-of-field dose generation and could be useful to build a framework that could minimize the generation of these doses in PT treatments.

Furthermore, the MiniPIX Timepix detector allowed us to perform a dose rate analysis as a function of time, which revealed the dose deposited as a function of the delivered layer. This analysis confirmed a dependence of out-of-field doses generation on the energy used by each layer, with higher energy layers, delivered first, exhibiting a higher dose rate. Such layer analysis cannot be performed using passive detectors such as bubble detectors-personal neutron dosimeter (BD-PND) or TLDs. Nevertheless, to establish a precise correlation between the time structures observed by the MiniPIX Timepix detector and those of the PBS system, it would be necessary to overlay the beam delivery log files with the dose rate analysis. This could be key information to elucidate biological effects, which amongst many other factors, also depend on the exposure duration and dose rate (Rühm et al., 2016). However, it should be highlighted that for such applications, Timepix3-based detectors are more suitable given their higher time resolution of 1.56 ns and decreased dead-time (Poikela et al., 2014; Shen et al., 2024).

Moreover, the absorbed dose in water measured by MiniPIX Timepix presented a good agreement with TOPAS simulations and TLD measurements for the two out-of-field positions farthest from the target, as well for the particle-specific absorbed dose estimated by MiniPIX Timepix and TOPAS. While the origin of protons may be different, including contributions from primary proton scattering, mostly for the nearest to the field position, and also secondary protons produced through inelastic nuclear interactions within the phantom and the detector sensor as well, both MiniPIX Timepix measurements and simulations confirmed that protons were the major contributor to the dose across all investigated positions. MiniPIX Timepix measurements showed that up to 87% of the absorbed dose across all the positions was delivered by protons. Concurrently, the relative contribution of heavier ions was shown to decrease with the distance from the isocenter, namely from 18% to 7.7%. Although heavier ions were not considered in the simulation of the absorbed dose presented here from the work of De Saint-Hubert *et al* (2022b), the measured dose by TLDs still accounted for these events. Still, the probability of these particles reaching the TLD detector is low, due to their short range. Even though, TLDs can be used to measure thermal neutrons, the sensitivity of MTS-7 detectors to neutrons is limited.

For position 1, an overestimation was observed in the MiniPIX Timepix measurements compared to the TOPAS simulations and TLD measurements, as well for the particle-specific absorbed dose estimated by MiniPIX Timepix and TOPAS. One possible factor that may explain this disagreement is the difference in the positions being evaluated with the MiniPIX Timepix detector compared to the simulations and TLD measurements. The MiniPIX Timepix position could not be compared to a TLD at exactly the same position. This because the MiniPIX Timepix required a replacement of CIRS slice by PMMA slice with an insert in the center while TLDs in that slice are positioned at 2

symmetric lateral positions (for thyroid measurement). However a comparison to a similar distance from the isocenter was made. This could be particularly challenging for Position 1, given the steep dose gradient at such close proximity.

Another contributing factor could be the variation in the sensitive volume size between the simulations and the MiniPIX Timepix measurements, with the former being nearly equivalent to the size of the TLDs, while the latter involved an averaging over a larger sensitive volume. Additionally, the replacement of the original phantom slices with customized-PMMA slices at positions where the MiniPIX Timepix measurements were performed may have also contributed to the observed differences. PMMA has a higher density and a different atomic composition compared to the original phantom material, which can result in increased local energy deposition from secondary charged particles due to the higher stopping power. Also, differences in the atomic composition can affect nuclear interaction cross sections, potentially altering the production and transport of secondary particles, including neutrons. On the other hand, pixel saturation due to proximity to the field was carefully avoided during measurements and it is therefore unlikely to have influenced this discrepancy.

Moving on to the total dose equivalent, a discrepancy was observed between the values simulated using TOPAS and those measured with the MiniPIX Timepix for positions 1 and 3. Specifically, an overestimation was observed at position 1, while an underestimation was observed at position 3. The overestimation at position 1, was already discussed as seen in the absorbed dose calculation, but one should also keep in mind differences in the methods used to calculate the total dose equivalent. The TOPAS simulations applied, an RBE of 1.1 for protons and an RBE of 1 for gammas, whereas the MiniPIX Timepix calculations used the LET dependent Q factor. These averaged Q values ranged between 1.01 and 1.11. Specifically for protons the average Q values ranged between 1.13 and 1.60.

Further away the proton dose will become less important as the neutron component will be dominant as seen in the study from De Saint-Hubert *et al* (2022b). For this reason, the underestimation at position 3 can be explained by the MiniPIX Timepix detector's low sensitivity to neutron measurements. The detector primarily relies on the direct detection of the protons and heavier ions created from interactions with the phantom material close to the sensor. Previous experiments tested the detection of fast and thermal neutrons with Timepix detectors, nevertheless these ones have used Timepix3 detectors with thin (~1 μm thick) neutron converter masks of ^{6}LiF and plastic polyethylene for thermal neutron and fast neutron conversion, respectively, these ones were mounted onto the sensor front side (Charyyev et al., 2023; Granja et al., 2023; Oancea, Solc, et al., 2023). In our work the phantom potentially could convert the neutrons into recoil protons but the sensitivity of our detector to neutrons has not been tested in detail. Moreover, the creation of short path length secondary charged particles in tissue/phantom materials cannot be properly modeled because the detector is not tissue equivalent and neutron interactions in Si are different and not representative to what would happen in tissue. Both the intrinsic neutron sensitivity of the detector and the contribution of recoil protons to the MiniPIX Timepix signal, remain to be characterized in detail for proper identification of neutrons in cluster patterns on the detector.

While the evaluation of the uncertainties associated with MiniPIX Timepix dose measurements is not straightforward as it involves several intermediate calculations, various sources of uncertainty can be identified. First, a positioning uncertainty of approximately ~2 mm, which by looking at MC data can result in an error on the absorbed dose between 10-25%, depending on the dose gradient in the measurement location. It is also important to carefully evaluate the dead-time and the accuracy of its correction method. Nonetheless, with the increasing shift towards newer chips such as Timepix 3 and Timepix 2, this is likely to become less of a concern. Furthermore, the errors associated with the dose conversion from silicon to water will depend on the particle type, LET estimation and any underlying assumptions. In the case of the stopping powers obtained from the NIST tables, uncertainties between 2% to 3% for electrons and 5% to 10% for protons and alpha particles can be found (Berger et al., 1999b). For protons, the experimental LET in water was found to agree with MC simulations within 14% (Nabha et al., 2023). For ions heavier than protons, the main limitation stems from grouping all particles into one class assumed to be alpha particles. While the ratio of stopping power in silicon and water is generally similar for different particles, fragmentation effects should not be overlooked (Parisi et al., 2022). Accurate particle identification is crucial for enhanced characterization and precise dose calculation in mixed radiation fields. The validation of the DPE revealed that approximately only 3% of events in each of the three classes considered in this work can be misidentified (Marek et al., 2024). It is important to note that, in practice, protons can have different origins (e.g. primary, neutron-induced recoil protons, or protons from (n, p) reactions in silicon), resulting in different energies and directions. Additionally, different heavy ions may have various track structures and biological effects. Exploring other cluster features, such as the incident and polar angles, LET and morphological parameters, will lead to a broader particle-type classification. Given the aforementioned considerations, more detailed uncertainty analysis will be performed to fully understand the capabilities and limitations of measurements with MiniPIX Timepix detectors. Currently, additional validation and testing of the DPE is underway to achieve a more precise particle identification. As this work progresses, it is expected that the accuracy and reliability of particle-type classification will improve, allowing for more accurate LET and dose calculations as well as conversion from silicon to water. The implications of the various sources of uncertainty can be different depending on the application, and the calculation of quantities of interest. Therefore, uncertainty analysis should also consider the required level of accuracy for specific applications.

The comparison with photon therapy techniques was beyond the scope of this study. Nevertheless, the benefits of PT were highlighted in another study with a similar experimental setup. Compared to three commonly used photon irradiation techniques, Knežević *et al (2022)* demonstrated that the total dose equivalent from PBS measured inside a phantom resembling a 5 year old was lower by one order of magnitude and more than two orders of magnitude close to and farther away from the target, respectively. The application of Timepix detectors has the potential to broaden comparable investigation to include various clinical indications (such as field configuration, range shifter, etc.) or susceptible patient groups, such as pregnant women (Michalet et al., 2022), to ensure the optimization of radiation protection. This technique may open a new perspective to study out-of-field doses for treatment optimization and improved radiation protection.

This study presents the use of a compact silicon-based Timepix detector to analyze in detail the total and particle-specific absorbed dose of a mixed radiation field in proton therapy. To the best of our knowledge, this is the first work that demonstrates the feasibility of estimating different dose quantities using a hybrid sensor in single-event mode with sufficient accuracy in out-of-field positions located farther from the target, validated with MC simulations and TLD measurements. In general, measuring the out-of-field dose requires a combination of detectors, some specifically designed for particular types of radiation, like neutrons or gammas. The MiniPIX Timepix detector may be a substitute for passive detectors such as TLDs for charged particles and photons. However, to have a full characterization of the mixed radiation field, this one could be combined with neutron dedicated detectors, such as bubble detectors, to measure the neutron component.. Furthermore, the measurements with this detector would not only provide dose values but can also provide detailed information for dose rate and particle identification.

5 Conclusion

In this work, we demonstrated the use of the compact MiniPIX Timepix detector for characterizing the mixed secondary radiation field in PT. Additionally, a method was presented to calculate particle-specific and total absorbed dose and dose equivalent in water. A good agreement was observed for the two farthest-locations from isocenter when comparing the absorbed dose in water estimated by the MiniPIX Timepix detector with TLD measurements and MC simulations. However, the closest position showed an overestimation for both the absorbed dose and the dose equivalent, while the farthest position exhibited an underestimation for the dose equivalent. This study demonstrates that the MiniPIX Timepix detector could reduce the need for combining multiple passive detector types or performing full MC simulations. However, it does not replace the need for neutron dedicated detectors when a complete assessment of the mixed radiation field is required. Detailed understanding and characterization of the secondary radiation field remains an important task to optimize planning for specific patient needs, particularly for pediatric patients and adults requiring reirradiation or treatment during pregnancy.

6 References

Ardenfors, O., Dasu, A., Lillhök, J., Persson, L., & Gudowska, I. (2018). Out-of-field doses from secondary radiation produced in proton therapy and the associated risk of radiation-induced cancer from a brain tumor treatment. *Physica Medica*, *53*, 129–136. https://doi.org/10.1016/J.EJMP.2018.08.020

Baiocco, G., Barbieri, S., Babini, G., Morini, J., Alloni, D., Friedland, W., Kundrát, P., Schmitt, E., Puchalska, M., Sihver, L., & Ottolenghi, A. (2016). The origin of neutron biological effectiveness as a function of energy. *Scientific Reports 2016 6:1*, *6*(1), 1–14. https://doi.org/10.1038/srep34033

Bäumer, C., Koska, B., Lambert, J., Timmermann, B., Mertens, T., & Talla, P. T. (2015). Evaluation of detectors for acquisition of pristine depth-dose curves in pencil beam scanning. *Journal of Applied Clinical Medical Physics*, *16*(6), 151–163. https://doi.org/10.1120/JACMP.V16I6.5577

Berger, M. J., Coursey, J. S., & Zucker, M. A. (1999a). *ESTAR, PSTAR, and ASTAR: Computer Programs for Calculating Stopping-Power and Range Tables for Electrons, Protons, and Helium Ions (version 1.21)*. https://www.nist.gov/publications/estar-pstar-and-astar-computer-programs-calculating-stopping-power-and-range-tables-0

Berger, M. J., Coursey, J. S., & Zucker, M. A. (1999b). *ESTAR, PSTAR, and ASTAR: Computer Programs for Calculating Stopping-Power and Range Tables for Electrons, Protons, and Helium Ions (version 1.21)*. https://www.nist.gov/publications/estar-pstar-and-astar-computer-programs-calculating-stopping-power-and-range-tables-0

Bisogni, M. G., Cirrone, G. A. P., Cuttone, G., Del Guerra, A., Lojacono, P., Piliero, M. A., Romano, F., Rosso, V., Sipala, V., & Stefanini, A. (2009). Medipix2 as a tool for proton beam characterization. *Nuclear Instruments and Methods in Physics Research Section A: Accelerators, Spectrometers, Detectors and Associated Equipment*, *607*(1), 48–50. https://doi.org/10.1016/J.NIMA.2009.03.115

Bortfeld, T. (1997). An analytical approximation of the Bragg curve for therapeutic proton beams. *Medical Physics*, *24*(12), 2024–2033. https://doi.org/10.1118/1.598116

Busse, P., Rosenthal, D. I., Hernandez, M., Swanson, D. M., Garden, A. S., Sturgis, E. M., Ferrarotto, R., Gunn, G. B., Patel, S. H., LEE, N. Y., Lin, A., Snider, J. W., McDonald, M. W., Henson, C., Bajaj, G. K., Kalman, N., Parvathaneni, U., Katz, S. R., Foote, R. L., & Consortium, M. A. C. T. (2024). Phase III randomized trial of intensity-modulated proton therapy (IMPT) versus intensity-modulated photon therapy (IMRT) for the treatment of head and neck oropharyngeal carcinoma (OPC). *Journal of Clinical Oncology*, *42*(16_suppl), 6006–6006. https://doi.org/10.1200/JCO.2024.42.16_SUPPL.6006

Byskov, C. S., Hansen, C. R., Dahlrot, R. H., Haldbo-Classen, L., Haslund, C. A., Kjær-Kristoffersen, F., Kristensen, T. O., Lassen-Ramshad, Y., Lukacova, S., Muhic, A., Nyström, P. W., Weber, B., & Kallehauge, J. F. (2021). Treatment plan comparison of proton vs photon radiotherapy for lower-grade gliomas. *Physics and Imaging in Radiation Oncology*, *20*, 98. https://doi.org/10.1016/J.PHRO.2021.11.008

Campbell, M., Heijne, E., Holý, T., Idárraga, J., Jakůbek, J., Lebel, C., Leroy, C., Llopart, X., Pospíšil, S., Tlustos, L., & Vykydal, Z. (2008). Study of the charge sharing in a silicon pixel detector by means of α-particles interacting with a Medipix2 device. *Nuclear Instruments and Methods in Physics Research Section A: Accelerators, Spectrometers, Detectors and Associated Equipment*, *591*(1), 38–41. https://doi.org/10.1016/J.NIMA.2008.03.096

Charyyev, S., Liu, R., Yang, X., Zhou, J., Dhabaan, A., Dynan, W. S., Oancea, C., & Lin, L. (2023). Measurement of the time structure of FLASH beams using prompt gamma rays and secondary neutrons as surrogates. *Physics in Medicine & Biology*, *68*(14), 145018. https://doi.org/10.1088/1361-6560/ACDC7C

Clasie, B., Depauw, N., Fransen, M., Gom, C., Panahandeh, H. R., Seco, J., Flanz, J. B., & Kooy, H. M. (2012). Golden Beam Data for Proton Pencil Beam Scanning. *Physics in Medicine and Biology*, *57*(5), 1147. https://doi.org/10.1088/0031-9155/57/5/1147

Clasie, B., Wroe, A., Kooy, H., Depauw, N., Flanz, J., Paganetti, H., & Rosenfeld, A. (2010). Assessment of out-of-field absorbed dose and equivalent dose in proton fields. *Medical Physics*, *37*(1), 311–321. https://doi.org/10.1118/1.3271390

Colson, D., Pinasti, S., Matamoros Ortega, A. N., De Saint-Hubert, M., Van Hoey, O., & Reniers, B. (2024). The influence of Monte Carlo radiation transport codes and hadron physics models on stray neutron dose estimations in proton therapy: An extended intercomparison. *Radiation Measurements*, *170*, 107046. https://doi.org/10.1016/J.RADMEAS.2023.107046

De Saint-Hubert, M., Farah, J., Klodowska, M., Romero-Expósito, M. T., Tyminska, K., Mares, V., Olko, P., Stolarczyk, L., & Trinkl, S. (2022). The influence of nuclear models and Monte Carlo radiation transport codes on stray neutron dose estimations in proton therapy. *Radiation Measurements*, *150*, 106693. https://doi.org/10.1016/J.RADMEAS.2021.106693

De Saint-Hubert, M., Verbeek, N., Bäumer, C., Esser, J., Wulff, J., Nabha, R., Van Hoey, O., Dabin, J., Stuckmann, F., Vasi, F., Radonic, S., Boissonnat, G., Schneider, U., Rodriguez, M., Timmermann, B., Thierry-Chef, I., & Brualla, L. (2022). Validation of a Monte Carlo Framework for Out-of-Field Dose Calculations in Proton Therapy. *Frontiers in Oncology*, *12*, 882489. https://doi.org/10.3389/FONC.2022.882489/BIBTEX

Englbrecht, F. S., Trinkl, S., Mares, V., Rühm, W., Wielunski, M., Wilkens, J. J., Hillbrand, M., & Parodi, K. (2021). A comprehensive Monte Carlo study of out-of-field secondary neutron spectra in a scanned-beam proton therapy gantry room. *Zeitschrift Für Medizinische Physik*, *31*(2), 215–228. https://doi.org/10.1016/J.ZEMEDI.2021.01.001

Faddegon, B., Ramos-Méndez, J., Schuemann, J., McNamara, A., Shin, J., Perl, J., & Paganetti, H. (2020). The TOPAS tool for particle simulation, a Monte Carlo simulation tool for physics, biology and clinical research. *Physica Medica*, *72*, 114–121. https://doi.org/10.1016/J.EJMP.2020.03.019

Gallagher, K. J., & Taddei, P. J. (2019). ANALYTICAL MODEL TO ESTIMATE EQUIVALENT DOSE FROM INTERNAL NEUTRONS IN PROTON THERAPY OF CHILDREN WITH INTRACRANIAL TUMORS. *Radiation Protection Dosimetry*, *183*(4), 460. https://doi.org/10.1093/RPD/NCY166

Gallagher, K. J., Youssef, B., Georges, R., Mahajan, A., Ann Feghali, J., Nabha, R., Ayoub, Z., Jalbout, W., & Taddei, P. J. (2021). Proton Radiotherapy Could Reduce the Risk of Fatal Second Cancers for Children with Intracranial Tumors in Low- and Middle-Income Countries. *International Journal of Particle Therapy*, *7*(4), 1. https://doi.org/10.14338/IJPT-20-00041.1

Gehrke, T., Burigo, L., Arico, G., Berke, S., Jakubek, J., Turecek, D., Tessonnier, T., Mairani, A., & Martišíková, M. (2017). Energy deposition measurements of single 1H, 4He and 12C ions of therapeutic energies in a silicon pixel detector. *Journal of Instrumentation*, *12*(04), P04025. https://doi.org/10.1088/1748-0221/12/04/P04025

Granja, C., Jakubek, J., Köster, U., Platkevic, M., & Pospisil, S. (2011). Response of the pixel detector Timepix to heavy ions. *Nuclear Instruments and Methods in Physics Research Section A: Accelerators, Spectrometers, Detectors and Associated Equipment*, *633*(SUPPL. 1), S198–S202. https://doi.org/10.1016/J.NIMA.2010.06.166

Granja, C., Jakubek, J., Polansky, S., Zach, V., Krist, P., Chvatil, D., Stursa, J., Sommer, M., Ploc, O., Kodaira, S., & Martisikova, M. (2018). Resolving power of pixel detector Timepix for wide-range electron, proton and ion detection. *Nuclear Instruments and Methods in Physics Research Section A: Accelerators, Spectrometers, Detectors and Associated Equipment*, *908*, 60–71. https://doi.org/10.1016/J.NIMA.2018.08.014

Granja, C., Jakubek, J., Soukup, P., Jakubek, M., Turecek, D., Marek, L., Oancea, C., Gohl, S., Bergmann, B., Pospisil, S., Malich, M., Vuolo, M., Owens, A., Zach, V., Stursa, J., Chvatil, D., Olsansky, V., Rucinski, A., Gajewski, J., … Solc, J. (2022). MiniPIX Timepix3 — a miniaturized radiation camera with onboard data processing for online characterization of wide-intensity mixed-radiation fields. *Journal of Instrumentation*, *17*(03), C03019. https://doi.org/10.1088/1748-0221/17/03/C03019

Granja, C., Kudela, K., Jakubek, J., Krist, P., Chvatil, D., Stursa, J., & Polansky, S. (2018). Directional detection of charged particles and cosmic rays with the miniaturized radiation camera MiniPIX Timepix. *Nuclear Instruments and Methods in Physics Research Section A: Accelerators, Spectrometers, Detectors and Associated Equipment*, *911*, 142–152. https://doi.org/10.1016/J.NIMA.2018.09.140

Granja, C., Oancea, C., Jakubek, J., Marek, L., Benton, E., Kodaira, S., Miller, J., Rucinski, A., Gajewski, J., Stasica, P., Zach, V., Stursa, J., Chvatil, D., & Krist, P. (2021). Wide-range tracking and LET-spectra of energetic light and heavy charged particles. *Nuclear Instruments and Methods in Physics Research Section A: Accelerators, Spectrometers, Detectors and Associated Equipment*, *988*, 164901. https://doi.org/10.1016/J.NIMA.2020.164901

Granja, C., Uhlar, R., Chuprakov, I., Alexa, P., Sansarbayar, E., Gledenov, Y. M., Poklop, D., Olsansky, V., Marek, L., Vuolo, M., & Pacik, J. (2023). Detection of fast neutrons with the pixel detector Timepix3. *Journal of Instrumentation*, *18*(01), P01003. https://doi.org/10.1088/1748-0221/18/01/P01003

Grassberger, C., Lomax, A., & Paganetti, H. (2014). Characterizing a proton beam scanning system for Monte Carlo dose calculation in patients. *Physics in Medicine & Biology*, *60*(2), 633. https://doi.org/10.1088/0031-9155/60/2/633

Gwosch, K., Hartmann, B., Jakubek, J., Granja, C., Soukup, P., Jäkel, O., & Martišíková, M. (2013). Non-invasive monitoring of therapeutic carbon ion beams in a homogeneous phantom by tracking of secondary ions. *Physics in Medicine & Biology*, *58*(11), 3755. https://doi.org/10.1088/0031-9155/58/11/3755

Hälg, R. A., & Schneider, U. (2020). Neutron dose and its measurement in proton therapy—current State of Knowledge. *The British Journal of Radiology*, *93*(1107). https://doi.org/10.1259/BJR.20190412

Jakubek, J. (2011). Precise energy calibration of pixel detector working in time-over-threshold mode. *Nuclear Instruments and Methods in Physics Research Section A: Accelerators, Spectrometers, Detectors and Associated Equipment*, *633*(SUPPL. 1), S262–S266. https://doi.org/10.1016/J.NIMA.2010.06.183

Jakubek, J., Granja, C., Jakel, O., Martisikova, M., & Pospicil, S. (2010). Detection and track visualization of primary and secondary radiation in hadron therapy beams with the pixel detector Timepix. *IEEE Nuclear Science Symposium Conference Record*, 1967–1969. https://doi.org/10.1109/NSSMIC.2010.5874118

Jarlskog, C. Z., & Paganetti, H. (2008). Physics settings for using the Geant4 toolkit in proton therapy. *IEEE Transactions on Nuclear Science*, *55*(3), 1018–1025. https://doi.org/10.1109/TNS.2008.922816

Knežević, Ambrozova, I., Domingo, C., De Saint-Hubert, M., Majer, M., Martínez-Rovira, I., Miljanić, S., Mojzeszek, N., Porwol, P., Ploc, O., Romero-Expósito, M., Stolarczyk, L., Trinkl, S., Harrison, R. M., & Olko, P. (2018). COMPARISON OF RESPONSE OF PASSIVE DOSIMETRY SYSTEMS IN SCANNING PROTON RADIOTHERAPY-A STUDY USING PAEDIATRIC ANTHROPOMORPHIC PHANTOMS. *Radiation Protection Dosimetry*, *180*(1–4), 256–260. https://doi.org/10.1093/RPD/NCX254

Knežević, Ž., Stolarczyk, L., Ambrožová, I., Caballero-Pacheco, M., Davídková, M., De Saint-Hubert, M., Domingo, C., Jeleń, K., Kopeć, R., Krzempek, D., Majer, M., Miljanić, S., Mojżeszek, N., Romero-Expósito, M., Martínez-Rovira, I., Harrison, R. M., & Olko, P. (2022). Out-of-Field Doses Produced

by a Proton Scanning Beam Inside Pediatric Anthropomorphic Phantoms and Their Comparison With Different Photon Modalities. *Frontiers in Oncology*, *12*, 1. https://doi.org/10.3389/FONC.2022.904563

Kry, S. F., Bednarz, B., Howell, R. M., Dauer, L., Followill, D., Klein, E., Paganetti, H., Wang, B., Wuu, C. S., & George Xu, X. (2017). AAPM TG 158: Measurement and calculation of doses outside the treated volume from external-beam radiation therapy. *Medical Physics*, *44*(10), e391–e429. https://doi.org/10.1002/MP.12462

Lai, P. T. C., Hai, V. H., & Phuc, N. T. T. (2025). Impacts of Geant4 hadronic physics models on secondary particle productions in proton therapy simulations. *Radiation Physics and Chemistry*, *229*, 112451. https://doi.org/10.1016/J.RADPHYSCHEM.2024.112451

Llopart, X., Ballabriga, R., Campbell, M., Tlustos, L., & Wong, W. (2007). Timepix, a 65k programmable pixel readout chip for arrival time, energy and/or photon counting measurements. *Nuclear Instruments and Methods in Physics Research Section A: Accelerators, Spectrometers, Detectors and Associated Equipment*, *581*(1–2), 485–494. https://doi.org/10.1016/J.NIMA.2007.08.079

Marek, L., Granja, C., Jakubek, J., Ingerle, J., Turecek, D., Vuolo, M., & Oancea, C. (2024). Data Processing Engine (DPE): data analysis tool for particle tracking and mixed radiation field characterization with pixel detectors Timepix. *Journal of Instrumentation*, *19*(04), C04026. https://doi.org/10.1088/1748-0221/19/04/C04026

Michalet, M., Dejean, C., Schick, U., Durdux, C., Fourquet, A., & Kirova, Y. (2022). Radiotherapy and pregnancy. *Cancer/Radiothérapie*, *26*(1–2), 417–423. https://doi.org/10.1016/J.CANRAD.2021.09.001

Mizumoto, M., Fuji, H., Miyachi, M., Soejima, T., Yamamoto, T., Aibe, N., Demizu, Y., Iwata, H., Hashimoto, T., Motegi, A., Kawamura, A., Terashima, K., Fukushima, T., Nakao, T., Takada, A., Sumi, M., Oshima, J., Moriwaki, K., Nozaki, M., … Sakurai, H. (2021). Proton beam therapy for children and adolescents and young adults (AYAs): JASTRO and JSPHO Guidelines. *Cancer Treatment Reviews*, *98*, 102209. https://doi.org/10.1016/J.CTRV.2021.102209

Nabha, R. (2023, May 24). *Biophysical characterization of primary and secondary radiation fields in proton therapy - KU Leuven*. https://kuleuven.limo.libis.be/discovery/fulldisplay?docid=lirias4083831&context=SearchWebhook&vid=32KUL_KUL:Lirias&lang=en&search_scope=lirias_profile&adaptor=SearchWebhook&tab=LIRIAS&query=any,contains,LIRIAS4083831&offset=0

Nabha, R., De Saint-Hubert, M., Marichal, J., Esser, J., Van Hoey, O., Bäumer, C., Verbeek, N., Struelens, L., Sterpin, E., Tabury, K., Marek, L., Granja, C., Timmermann, B., & Vanhavere, F. (2023). Biophysical characterization of collimated and uncollimated fields in pencil beam scanning proton therapy. *Physics in Medicine & Biology*, *68*(6), 064001. https://doi.org/10.1088/1361-6560/ACBE8D

Nabha, R., Van Hoey, O., Granja, C., Parisi, A., De Saint-Hubert, M., Struelens, L., Oancea, C., Sterpin, E., Zach, V., Stursa, J., Rucinski, A., Gajewski, J., Stasica, P., & Vanhavere, F. (2022). A novel method to assess the incident angle and the LET of protons using a compact single-layer Timepix detector. *Radiation Physics and Chemistry*, *199*, 110349. https://doi.org/10.1016/J.RADPHYSCHEM.2022.110349

Newhauser, W. D., & Durante, M. (2011). Assessing the risk of second malignancies after modern radiotherapy. *Nat Rev Cancer*, *11*(6), 438–448. https://doi.org/10.1038/nrc3069

Newhauser, W. D., Fontenot, J. D., Mahajan, A., Kornguth, D., Stovall, M., Zheng, Y., Taddei, P. J., Mirkovic, D., Mohan, R., Cox, J. D., & Woo, S. (2009). The risk of developing a second cancer after receiving craniospinal proton irradiation. *Physics in Medicine & Biology*, *54*(8), 2277. https://doi.org/10.1088/0031-9155/54/8/002

Newhauser, W. D., Schneider, C., Wilson, L., Shrestha, S., & Donahue, W. (2018). A REVIEW OF ANALYTICAL MODELS OF STRAY RADIATION EXPOSURES FROM PHOTON- AND PROTON-BEAM RADIOTHERAPIES. *Radiation Protection Dosimetry*, *180*(1–4), 245–251. https://doi.org/10.1093/RPD/NCX245

Oancea, C., Granja, C., Marek, L., Jakubek, J., Šolc, J., Bodenstein, E., Gantz, S., Pawelke, J., & Pivec, J. (2023). Out-of-field measurements and simulations of a proton pencil beam in a wide range of dose rates using a Timepix3 detector: Dose rate, flux and LET. *Physica Medica*, *106*, 102529. https://doi.org/10.1016/J.EJMP.2023.102529

Oancea, C., Solc, J., Bourgouin, A., Granja, C., Jakubek, J., Pivec, J., Riemer, F., Vykydal, Z., Worm, S., & Marek, L. (2023). Thermal neutron detection and track recognition method in reference and out-of-field radiotherapy FLASH electron fields using Timepix3 detectors. *Physics in Medicine & Biology*, *68*(18), 185017. https://doi.org/10.1088/1361-6560/ACF2E1

Opalka, L., Granja, C., Hartmann, B., Jakubek, J., Jaekel, O., Martisikova, M., Pospisil, S., & Solc, J. (2012). 3D measurement of the radiation distribution in a water phantom in a hadron therapy beam. *Journal of Instrumentation*, *7*(01), C01085. https://doi.org/10.1088/1748-0221/7/01/C01085

Opalka, L., Granja, C., Hartmann, B., Jakubek, J., Jaekel, O., Martisikova, M., Pospisil, S., & Solc, J. (2013). Linear energy transfer and track pattern recognition of secondary radiation generated in hadron therapy beam in a PMMA target. *Journal of Instrumentation*, *8*(02), C02047. https://doi.org/10.1088/1748-0221/8/02/C02047

Parisi, A., Olko, P., Swakoń, J., Horwacik, T., Jabłoński, H., Malinowski, L., Nowak, T., Struelens, L., & Vanhavere, F. (2022). Microdosimetric characterization of a clinical proton therapy beam: comparison between simulated lineal energy distributions in spherical water targets and experimental measurements with a silicon detector. *Physics in Medicine & Biology*, *67*(1), 015006. https://doi.org/10.1088/1361-6560/AC4563

Perl, J., Shin, J., Schümann, J., Faddegon, B., & Paganetti, H. (2012). TOPAS: An innovative proton Monte Carlo platform for research and clinical applications. *Medical Physics*, *39*(11), 6818. https://doi.org/10.1118/1.4758060

PIXet - ADVACAM Wiki. (n.d.). Retrieved September 18, 2024, from https://wiki.advacam.cz/index.php/PIXet

Poikela, T., Plosila, J., Westerlund, T., Campbell, M., Gaspari, M. De, Llopart, X., Gromov, V., Kluit, R., Beuzekom, M. Van, Zappon, F., Zivkovic, V., Brezina, C., Desch, K., Fu, Y., & Kruth, A. (2014). Timepix3: a 65K channel hybrid pixel readout chip with simultaneous ToA/ToT and sparse readout. *Journal of Instrumentation*, *9*(05), C05013. https://doi.org/10.1088/1748-0221/9/05/C05013

Reinhart, A. M., Spindeldreier, C. K., Jakubek, J., & Martišíková, M. (2017). Three dimensional reconstruction of therapeutic carbon ion beams in phantoms using single secondary ion tracks. *Physics in Medicine & Biology*, *62*(12), 4884. https://doi.org/10.1088/1361-6560/AA6AEB

Romero-Expósito, M., Domingo, C., Sánchez-Doblado, F., Ortega-Gelabert, O., & Gallego, S. (2016). Experimental evaluation of neutron dose in radiotherapy patients: Which dose? *Medical Physics*, *43*(1), 360–367. https://doi.org/10.1118/1.4938578

Rosenfeld, A., Alnaghy, S., Petasecca, M., Cutajar, D., Lerch, M., Pospisil, S., Giacometti, V., Schulte, R., Rosso, V., Würl, M., Granja, C., Martišíková, M., & Parodi, K. (2020). Medipix detectors in radiation therapy for advanced quality-assurance. *Radiation Measurements*, *130*, 106211. https://doi.org/10.1016/J.RADMEAS.2019.106211

Rühm, W., Azizova, T. V., Bouffler, S. D., Little, M. P., Shore, R. E., Walsh, L., & Woloschak, G. E. (2016). Dose-rate effects in radiation biology and radiation protection. *Https://Doi.Org/10.1177/0146645316629336*, *45*, 262–279. https://doi.org/10.1177/0146645316629336

Schneider, U., Agosteo, S., Pedroni, E., & Besserer, J. (2002). Secondary neutron dose during proton therapy using spot scanning. *International Journal of Radiation Oncology*Biology*Physics*, *53*(1), 244–251. https://doi.org/10.1016/S0360-3016(01)02826-7

Schneider, U., Hälg, R. A., & Lomax, T. (2017). Neutrons in active proton therapy: Parameterization of dose and dose equivalent. *Zeitschrift Für Medizinische Physik*, *27*(2), 113–123. https://doi.org/10.1016/J.ZEMEDI.2016.07.001

Shen, J., Ding, X., Charyyev, S., Liang, X., Oancea, C., Wang, P., Rule, W. G., Liu, W., Bues, M., & Lin, L. (2024). Time structures of proton pencil beam scanning delivery on a microsecond scale measured with a pixelated semiconductor detector Timepix3. *Journal of Applied Clinical Medical Physics*, *25*(9), e14486. https://doi.org/10.1002/ACM2.14486

Shrestha, S., Newhauser, W. D., Donahue, W. P., & Pérez-Andújar, A. (2022). Stray neutron radiation exposures from proton therapy: physics-based analytical models of neutron spectral fluence, kerma and absorbed dose. *Physics in Medicine & Biology*, *67*(12), 125019. https://doi.org/10.1088/1361-6560/AC7377

Sommer, M., Granja, C., Kodaira, S., & Ploc, O. (2022). High-energy per-pixel calibration of timepix pixel detector with laboratory alpha source. *Nuclear Instruments and Methods in Physics Research Section A: Accelerators, Spectrometers, Detectors and Associated Equipment*, *1022*, 165957. https://doi.org/10.1016/J.NIMA.2021.165957

Stasica, P., Baran, J., Granja, C., Krah, N., Korcyl, G., Oancea, C., Pawlik-Niedźwiecka, M., Niedźwiecki, S., Rydygier, M., Schiavi, A., Rucinski, A., & Gajewski, J. (2020). A Simple Approach for Experimental Characterization and Validation of Proton Pencil Beam Profiles. *Frontiers in Physics*, *8*, 567825. https://doi.org/10.3389/FPHY.2020.00346/BIBTEX

Stolarczyk, L., Trinkl, S., Romero-Expósito, M., Mojzeszek, N., Ambrozova, I., Domingo, C., Davidková, M., Farah, J., Kłodowska, M., Knežević, Liszka, M., Majer, M., Miljanić, S., Ploc, O., Schwarz, M., Harrison, R. M., & Olko, P. (2018). Dose distribution of secondary radiation in a water phantom for a proton pencil beam—EURADOS WG9 intercomparison exercise. *Physics in Medicine & Biology*, *63*(8), 085017. https://doi.org/10.1088/1361-6560/AAB469

Taddei, P. J., Mirkovic, D., Fontenot, J. D., Giebeler, A., Zheng, Y., Kornguth, D., Mohan, R., & Newhauser, W. D. (2009). Stray radiation dose and second cancer risk for a pediatric patient receiving craniospinal irradiation with proton beams. *Physics in Medicine & Biology*, *54*(8), 2259. https://doi.org/10.1088/0031-9155/54/8/001

Thomas, H., & Timmermann, B. (2020). Paediatric proton therapy. *The British Journal of Radiology*, *93*(1107). https://doi.org/10.1259/BJR.20190601

Vedelago, J., Geser, F. A., Munoz, I. D., Stabilini, A., Yukihara, E. G., & Jakel, O. (2022). Assessment of secondary neutrons in particle therapy by Monte Carlo simulations. *Physics in Medicine & Biology*, *67*(1), 015008. https://doi.org/10.1088/1361-6560/AC431B

Verbeek, N., Wulff, J., Bäumer, C., Smyczek, S., Timmermann, B., & Brualla, L. (2021). Single pencil beam benchmark of a module for Monte Carlo simulation of proton transport in the PENELOPE code. *Medical Physics*, *48*(1), 456–476. https://doi.org/10.1002/MP.14598

Wieser, H. P., Cisternas, E., Wahl, N., Ulrich, S., Stadler, A., Mescher, H., Muller, L. R., Klinge, T., Gabrys, H., Burigo, L., Mairani, A., Ecker, S., Ackermann, B., Ellerbrock, M., Parodi, K., Jakel, O., & Bangert, M. (2017). Development of the open-source dose calculation and optimization toolkit matRad. *Medical Physics*, *44*(6), 2556–2568. https://doi.org/10.1002/MP.12251

Xiang, M., Chang, D. T., & Pollom, E. L. (2020). Second cancer risk after primary cancer treatment with three-dimensional conformal, intensity-modulated, or proton beam radiation therapy. *Cancer*, *126*(15), 3560–3568. https://doi.org/10.1002/CNCR.32938

Yonekura, Y., Tsujii, H., Hopewell, J. W., LÃƒÂ³pez, P. O., Cosset, J. M., Paganetti, H., Montelius, A., Schardt, D., Jones, B., & Nakamura, T. (2014). ICRP Publication 127: Radiological Protection in Ion Beam Radiotherapy. *Annals of the ICRP*, *43*(4), 5–113. https://doi.org/10.1177/0146645314559144

Zacharatou Jarlskog, C., Lee, C., Bolch, W. E., Xu, X. G., & Paganetti, H. (2008). Assessment of organ-specific neutron equivalent doses in proton therapy using computational whole-body age-dependent voxel phantoms. *Physics in Medicine & Biology*, *53*(3), 693. https://doi.org/10.1088/0031-9155/53/3/012

Zhang, R., Howell, R. M., Giebeler, A., Taddei, P. J., Mahajan, A., & Newhauser, W. D. (2013). Comparison of risk of radiogenic second cancer following photon and proton craniospinal irradiation for a pediatric medulloblastoma patient. *Physics in Medicine & Biology*, *58*(4), 807. https://doi.org/10.1088/0031-9155/58/4/807